RESEARCH ARTICLE





Two- and one-photon absorption spectra of aqueous thiocyanate anion highlight the role of symmetry in the condensed phase

Ronit Sarangi 🕒 | Kaushik D. Nanda 🕒 | Anna I. Krylov 🗅

Department of Chemistry, University of Southern California, Los Angeles, California, USA

Anna I. Krylov, Department of Chemistry, University of Southern California, Los Angeles, CA 90089, USA.

Email: krylov@usc.edu

Abstract

We present the two-photon absorption (2PA) spectrum of aqueous thiocyanate calculated using high-level quantum-chemistry methods. The 2PA spectrum is compared to the one-photon absorption (1PA) spectrum computed using the same computational protocol. Although the two spectra probe the same set of electronic states, the intensity patterns are different, leading to an apparent red-shift of the 2PA spectrum relative to the 1PA spectrum. The presented analysis explains the intensity patterns and attributes the differences between the 1PA and 2PA spectra to the native symmetry of isolated SCN-, which influences the spectra in the lowsymmetry solvated environment. The native symmetry also manifests itself in variations of the polarization ratio (e.g., parallel vs. perpendicular cross sections) across the spectrum. The presented results highlight the potential of 2PA spectroscopy and high-level quantum-chemistry methods in studies of condensed-phase phenomena.

KEYWORDS

charge-transfer-to-solvent states, computational spectroscopy, equation-of-motion coupledcluster, molecular orbital theory, two-photon spectroscopy, wave-function analysis

INTRODUCTION

Spectroscopy in the condensed phase reveals both the electronic structure of solvated molecules and the details of the local solvent structure around the solute. Particularly sensitive to the solvent structure are the charge-transfer-to-solvent (CTTS) states. 1-3 These states, common for anionic solutes, are derived by promoting an electron from a molecular orbital to a proximal solvent cavity. The shapes of the molecular orbitals occupied by the excited electron resemble solvated electrons; however, in CTTS states, the excited electron interacts with the molecular core, making these states optically accessible. They appear as broad and featureless bands in the deep ultraviolet (UV) region (above 5 eV) of many solvated anions. Because of the diffuse character of the excited electron, the energies and oscillator strengths of CTTS states depend strongly on the size and shape of the solvent cavity around the solute. Importantly, these states are highly sensitive to dynamic structural fluctuations of the solvent around the solute. This sensitivity

leads to the strong solvent, temperature, and pressure dependence of the CTTS bands.^{3,4} Furthermore, owing to this sensitivity, spectroscopies involving CTTS states can be used to probe the local structure of the solvent around anions and its dynamic fluctuations. However, to relate experimental spectra to microscopic structural information, theoretical modeling is required.

Recently, we presented a computational study of aqueous thiocyanate⁵ using high-level electronic structure methods. We investigated the sensitivity of the computed UV-visible (UV-vis) spectra to the details of computational protocol, in particular, equilibrium sampling. We found that molecular dynamics (MD) simulations using classical force fields produced more confined local structures around the thiocyanate anions as compared to more reliable simulations using ab initio MD (AIMD) combined with electrostatic embedding. Consequently, the spectra computed using these two sets of snapshots were markedly different, despite the inhomogeneous broadening of the transitions. Thus,

the combination of theory and experiments can be used to validate and improve theoretical methods for condensed-phase modeling.

In this contribution, we compute and analyze the two-photon absorption (2PA) spectrum of $\mathsf{SCN}^-_{(\mathsf{aq})}$ using the same computational protocol as in our previously reported calculations of the one-photon absorption (1PA) spectrum. Nonlinear spectroscopies, such as 2PA, second-harmonic generation, and electronic sum-frequency generation (SFG), are gaining popularity, including applications to solvated anions.⁶⁻¹⁰ Because 1PA and 2PA transitions are governed by different selection rules, 2PA spectra can provide complementary information, for example, by revealing states that are dark in 1PA. 11,12 In addition, 2PA can provide more detailed information about the underlying electronic structure, such as the symmetry of electronic states of the solute, by varying the polarizations of the two photons. 12-14 For example, Bradforth and co-workers have shown that different electronic states of water can be discerned from polarization dependence of the continuous 2PA spectra of bulk water. 15

Although in the condensed phase the formal symmetry is C_1 , the native symmetry of the solvated species strongly influences their optical properties. For example, $n \to \pi^*$ transitions are rather dim in 1PA, despite being formally allowed. However, such dim transitions can be probed using a different spectroscopy. As a recent illustration of how 1PA selection rules can be overcome by multiphoton techniques, consider the electronic spectrum of aqueous OH radical. Its UV-vis spectrum shows only a small shoulder corresponding to the $\sigma(p_z) \to \pi(p_x/p_y)$ valence transition, but the same transitions become sharp and intense in the RIXS (resonant inelastic x-ray scattering) spectrum. If

As a linear molecule, SCN⁻ is an interesting model system for analyzing the effect of native symmetry on the 1PA and 2PA spectra in solutions. Here, we analyze the computed electronic states and their properties in terms of their relationship to hypothetical states of an ideal symmetric model. By comparing the 1PA and 2PA spectra, we highlight the differences in their intensity patterns. Together with polarization data, such differences between the 1PA and 2PA spectra can be used for spectroscopic assignments. We hope that our simulations will motivate experimental efforts to measure the continuous 2PA spectrum of this interesting system.

The structure of the paper is as follows. We begin with a description of theoretical methods and computational protocols. We then discuss the molecular orbital (MO) framework and introduce symmetry analysis of the low-energy electronic states of aqueous thiocyanate. Using this analysis, we then explain the trends in the computed 1PA and 2PA spectra.

2 | THEORETICAL METHODS AND COMPUTATIONAL DETAILS

Ab initio modeling of condensed-phase spectroscopy requires the following: (i) a quantum chemistry method capable of describing

electronic states involved; (ii) an adequate description of the solute-solvent interactions; (iii) the ability to compute spectroscopic signal (e.g., absorption cross sections); (iv) reliable description of equilibrium dynamics; and (v) tools for spectroscopic assignments. Our previous study of aqueous thiocyanate⁵ illustrates the challenges involved in developing computationally feasible protocols that adequately address these points. Below, we briefly summarize essential details of the theoretical framework and its extension to 2PA.

We use the equation-of-motion coupled-cluster method for electronically excited states with single and double substitutions (EOM-EE-CCSD), which is capable of treating states of different character (e.g., local and CTTS excitations) in a balanced way. Describing solvent effects in calculations of electronic spectra of solvated anions is particularly difficult because, in addition to strong electrostatic interactions, one should also properly treat quantum-confinement effects (Pauli repulsion between solvent molecules and excited electrons) that prevent the artificial spilling of the electron density of the solute into the solvent. Towards this end, we employ a relatively large QM system comprising the thiocyanate molecule and more than two solvation shells.

Whereas calculating UV-vis (1PA) intensities are straightforward, calculating the 2PA cross sections requires implementation of response equations. Here, we use the theoretical framework described in References 18–20. We carried out equilibrium averaging using the same snapshots from the AIMD trajectories as were used in the calculations of 1PA spectra. To assign spectral features, we used wave-function analysis and exciton descriptors, 11–25 in particular, exciton sizes, which allow one to distinguish between local and CTTS excitations. For 2PA, we used the NTOs of the response density matrices, which are related to the 2PA transition moments.

We note that modeling of multiphoton properties such as 2PA cross sections is very sensitive to approximations in electron-correlation treatment. The underlying model Hamiltonians must reliably describe not only the initial and final states in a transition but the full spectrum of electronic states, owing to the sum-over-states expressions of the corresponding cross sections (see, for example, expressions for the 2PA transition moments below). This is different from modeling one-photon spectroscopies (e.g., UV-vis) in which one only needs to compute transition dipole moments between the ground state and a few low-lying excited states. Therefore, electronic structure methods and computational protocols that provide a robust theoretical characterization of UV-vis spectra may be inadequate for 2PA spectra. The sector of the corresponding of the sum-over-states and a few low-lying excited states.

EOM-EE-CCSD has been used to model 2PA spectra of several isolated chromophores, ^{18,27-30} showing a reasonable agreement with available experimental spectra despite neglecting the solvent effects, especially in non-polar solvents. ^{28,29} Coupled-cluster simulations using explicit solvent models have also been reported. ^{19,31,32} Here, we apply the EOM-EE-CCSD method combined with an explicit solvent treatment to a system that is more demanding in terms of the description of the solute–solvent interactions. This is the first application of EOM-EE-CCSD for calculations of nonlinear optical spectra involving CTTS states. Once the experimental 2PA spectrum of

 $SCN^-_{(aq)}$ becomes available, our simulations will serve as an important benchmark for assessing the performance of EOM-EE-CCSD combined with the explicit description of the solvent. These results can also be used for developing more approximate treatments for electron correlation and embedding.

2.1 | 2PA cross sections within EOM-EE-CCSD framework

Below, we outline the theoretical framework for computing 2PA cross sections.
¹⁸ Within the non-Hermitian EOM-CC theory, the right and left transition moments are not equivalent. Using the expectation-value EOM-EE-CCSD formalism, the right and left 2PA transition moments $(M_{yz}^{f-g}$ and M_{yz}^{g-f} , respectively) are given by the sum-over-all-states expressions, ¹⁸⁻²⁰

$$\begin{split} M_{\gamma z}^{f \leftarrow g} &= -\sum_{n} \frac{\langle \Phi_{0} | \hat{L}^{f} \widehat{\mu}_{z} \hat{R}^{n} | \Phi_{0} \rangle \langle \Phi_{0} | \hat{L}^{n} \widehat{\mu}_{y} \hat{R}^{g} | \Phi_{0} \rangle}{E^{n} - E^{g} - \omega_{1}} \\ &- \sum_{n} \frac{\langle \Phi_{0} | \hat{L}^{f} \widehat{\mu}_{y} \hat{R}^{n} | \Phi_{0} \rangle \langle \Phi_{0} | \hat{L}^{n} \widehat{\mu}_{z} \hat{R}^{g} | \Phi_{0} \rangle}{E^{n} - E^{g} - \omega_{2}} \end{split} \tag{1}$$

and

$$\begin{split} M_{yz}^{g-f} &= -\sum_{n} \frac{\langle \Phi_{0} | \widehat{L}^{g} \widehat{\overline{\mu}}_{y} \widehat{R}^{n} | \Phi_{0} \rangle \langle \Psi_{0} | \widehat{L}^{n} \widehat{\overline{\mu}}_{z} \widehat{R}^{f} | \Phi_{0} \rangle}{E^{n} - E^{g} - \omega_{1}} \\ &- \sum_{n} \frac{\langle \Phi_{0} | \widehat{L}^{g} \widehat{\overline{\mu}}_{z} \widehat{R}^{n} | \Phi_{0} \rangle \langle \Phi_{0} | \widehat{L}^{n} \widehat{\overline{\mu}}_{y} \widehat{R}^{f} | \Phi_{0} \rangle}{E^{n} - E^{g} - \omega_{2}}. \end{split} \tag{2}$$

Here, g, n, and f are state indices for the initial, intermediate, and final states. The energies E^k and right and left EOM-CC wave functions $(\hat{R}^k|\Phi_0)$ and $\langle\Phi_0|\hat{L}^k$, respectively) of state k within the EOM-EE-CCSD framework are computed by solving the following right and left EOM-CC eigenvalue equations in the determinant space of the reference (Φ_0) and singly and doubly excited determinants:

$$\overline{H}\hat{R}^{k}|\Phi_{0}\rangle = E^{k}\hat{R}^{k}|\Phi_{0}\rangle \tag{3}$$

and

$$\langle \Phi_0 | \hat{L}^k \overline{H} = \langle \Phi_0 | \hat{L}^k E^k, \tag{4}$$

where $\overline{H}=e^{-\hat{T}}He^{\hat{T}}$ is the EOM-CCSD similarity-transformed Hamiltonian expressed in terms of the CCSD operator, \hat{T} . The energies of the two photons (ω s) satisfy the 2PA resonance condition: $\Omega^{fg}=E^f-E^g=\omega_1+\omega_2$. $\widehat{\mu}_{\chi}=e^{-\hat{T}}\overline{\mu}_{\chi}e^{\hat{T}}$ is the x Cartesian component of the similarity-transformed dipole-moment operator. The 2PA transition moments are computed by recasting the sum-over-states expressions into expressions that use response wave functions, which can be computed with roughly the same cost as excited-state wave functions themselves. 18

The rotationally averaged microscopic 2PA cross sections are computed using the transition strength matrix, $S_{ab,cd}$, as follows:

$$\begin{split} \left\langle \delta^{2PA} \right\rangle^{gf} &= \frac{1}{30} (F \delta_F + G \delta_G + H \delta_H) \\ &= \frac{1}{30} \Biggl(F \sum_{a,b} S^{gf}_{aa,bb} + G \sum_{a,b} S^{gf}_{ab,ab} + H \sum_{a,b} S^{gf}_{ab,ba} \Biggr), \end{split} \tag{5}$$

where $S_{ab,cd}$ is given in terms of the products of left and right 2PA transition-moment components,

$$S_{ab,cd}^{gf} = \frac{1}{2} \left(\left(M_{ab}^{g-f} \right)^* M_{cd}^{f-g} + \left(M_{cd}^{g-f} \right)^* M_{ab}^{f-g} \right). \tag{6}$$

The constants F, G, and H depend on the polarization of the incident light. $^{13}F=G=H=2$ for parallel linearly polarized light, F=-1, G=4, H=-1 for perpendicular linearly polarized light, and F=-2, G=H=3 for circularly polarized light.

The macroscopic 2PA cross sections, $\langle \sigma^{2PA} \rangle$ (in Göppert-Mayer units, 1 GM $= 10^{-50}$ cm⁴s/photon) are expressed in terms of $\langle \delta^{2PA} \rangle$ as

$$\left\langle \sigma^{\text{2PA}}\right\rangle^{\text{gf}}(\omega) = \frac{2\pi^3 \alpha a_0^5 \left(\Omega^{\text{fg}}\right)^2}{c} \left\langle \delta^{\text{2PA}}\right\rangle^{\text{g--f}} \mathscr{L}\left(\Omega^{\text{fg}}, \omega, \Gamma\right), \tag{7}$$

where α is the fine structure constant, a_0 is the Bohr radius, c is the speed of light, and $\mathcal{L}(E^f - E^g, \omega, \Gamma)$ is the lineshape function (Γ is an empirical factor describing line broadening).

A typical experimental setup for measuring 2PA spectra involves a non-resonant pump and broad-band probe beams, $^{15,28-30}$ meaning that ω_1 is fixed and $\omega_2 = E_{ex} - \omega_1$.

2.2 | Polarization ratios

In their pioneering work, McClain and co-workers^{13,14} explained that by varying relative polarization of the two photons, one can discern the three contributions to the overall cross-section— δ_F , δ_G , and δ_H —and by doing so gain a more detailed picture of the underlying electronic structure. The most common approach is to compare the spectra obtained with parallel (σ_{par}) and perpendicular (σ_{perp}) polarizations of the two photons. Below we briefly summarize the key expressions.¹³

For linearly polarized light,

$$\langle \delta \rangle = A + B\cos^2(\theta),$$
 (8)

where θ is the angle between the two photons. Hence, the polarization ratio r of parallel and perpendicular cross sections is

$$r = \frac{\delta_{par}}{\delta_{perp}} = 1 + \frac{B}{A}.$$
 (9)

For the degenerate 2PA, $\delta_{\rm G}=\delta_{\rm H}$ (this also holds for non-degenerate case for fully symmetric transitions).¹³ In these cases,

$$A = -\delta_F + 3\delta_G, \tag{10}$$

$$B = 3\delta_F + \delta_G. \tag{11}$$

As per Equation (5), the expressions for δ_F and δ_G are:

$$\delta_{F} = \sum_{a,b} S_{aa,bb} = S_{xx,xx} + S_{xx,yy} + S_{xx,zz} + S_{yy,xx} + S_{yy,zz} + S_{yy,zz} + S_{zz,yx} + S_{zz,yy} + S_{zz,zz}$$
(12)

and

$$\delta_{G} = \sum_{a,b} S_{ab,ab} = S_{xx,xx} + S_{xy,xy} + S_{xz,xz} + S_{yx,yx} + S_{yy,yy} + S_{yz,yz} + S_{zx,zx} + S_{zy,zy} + S_{zz,zz}.$$
(13)

To apply these equations to a specific case, one needs to write down the structure of $S_{ab,cd}$ based on the properties of the 2PA moments (they are given in Reference 14 for all symmetry groups). Below we do this for SCN⁻ ($C_{\infty V}$).

2.3 | Computational details

We computed the 2PA spectra using a hybrid QM/MM approach with an electrostatic embedding scheme in which the QM part was treated with EOM-EE-CCSD and the MM waters were described as Gaussianbroadened TIP3P point charges. As in the previous calculations of 1PA spectra, we constructed the spectra using eight excited states per snapshot (the benchmarks in Reference 5 have shown that the computed 1PA spectrum does not change when up to 10 states per snapshot were computed). A total of 40 snapshots were chosen from the AIMD calculations performed in Reference 5. The QM region consisted of SCN⁻ and 20 nearest waters with the 6-31+G* basis on the anion and 11 nearest waters and 6-31G on the rest. We carried out non-degenerate 2PA calculations with ω_1 fixed at 4.66 eV (pump of 266 nm is often used in multiphoton spectroscopies 10). The lineshape function, \mathcal{L} , was a normalized Gaussian with FWHM of 0.1 eV. All calculations were performed using the Q-Chem software. 33,34 We provide a sample input for EOM-EE-CCSD 2PA jobs in the SI.

3 | RESULTS AND DISCUSSION

We begin with discussing the MO framework and symmetry of the electronic states of SCN $^-$. Although in the condensed phase the symmetry is C_1 , MOs largely retain their shapes and nodal structures, as can be easily seen from the computed orbitals; for example, Figure 3 in Reference 5 and Tables S1 and S2 in the SI. Thus, the electronic states of SCN $^-_{(aq)}$ can be understood in terms of perturbed states of an isolated linear molecule.

Table 1 shows the character table for $C_{\infty V}$ group. It has an infinite number of irreducible representations (irreps), but for the low-lying electronic states of SCN $^-$ only A_1 , A_2 , E_1 , and E_2 are relevant. Figure 1 shows the MOs involved in the low-lying electronic transitions of SCN $^-$: doubly degenerate HOMO of π character (E_1/Π), doubly

TABLE 1 Character table for $C_{\infty V}$ group with standard and spectroscopic irrep labels.

Irrep	Ε	2C _∞	$\infty \sigma_{V}$	Lin. fns.
A_1/Σ^+	1	1	1	Z
A_2/Σ^-	1	1	-1	
E_1/Π	1	$2\cos(\phi)$	0	x,y
E_2/Δ	1	$2\cos(2\phi)$	0	
E_3/Φ	1	$2\cos(3\phi)$	0	
En	1	$2\cos(n\phi)$	0	

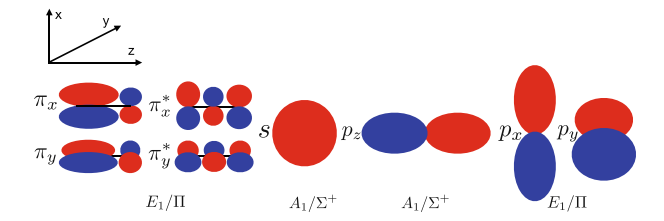


FIGURE 1 Relevant molecular orbitals of SCN $^-$ and their symmetry labels (in $C_{\infty v}$ group).

degenerate LUMO of π^* character (E_1/Π), and four diffuse atomic-like orbitals—s (A_1/Σ^+), p_z (A_1/Σ^+), and p_x/p_y (E_1/Π).

The ground electronic state of SCN $^-$ is $X^1\Sigma^+$. Isolated thiocyanate anion does not support bound electronic excited states, but in aqueous solutions the detachment energy increases considerably and several excited states become electronically bound. The low-lying states of aqueous SCN $^-$ are derived from the transitions between the doubly degenerate π HOMO and doubly degenerate π^* LUMO, giving rise to the intra-molecular excitations, and transitions from the HOMO to the diffuse atomic-like orbitals (s, p_x , p_y , and p_z), giving rise to the CTTS transitions. The CTTS transitions can mix with the locally excited transitions. In the absence of symmetry, all transitions can mix, however, as we observe from the calculations, many states have character that can be assigned to a particular type of transition. This can be seen from the shapes of NTOs, and even more so, from the electronic properties (e.g., oscillator strengths). As we show below, this native symmetry also explains trends in the 2PA spectrum.

Table 2 shows the symmetries of electronic states derived from transitions between orbitals from Figure 1 (see Table S1 in the SI for the irrep multiplication table). There are a total of twelve configurations that can be generated of which six are dipole allowed—one local transition and five CTTS transitions. We note that the NTO analysis only shows the nature of the orbitals involved, but does not distinguish between different symmetries—for example, all local excitations have two pairs of similar looking NTOs. Different states can be distinguished by either wave-function amplitudes or by the transition properties such as transition dipole moments or matrix elements of the angular momentum operator.

The calculations of the spectra are based on eight lowest exited states, which was deemed sufficient for capturing the low-energy part

of the 1PA spectrum. ⁵ Figure 2 shows the computed density of states and the 1PA spectrum. As one can see, the eight states span an energy range of about 2 eV and are clustered in three groups—around 5.7, 6.5, and 7.2 eV, with the second group being the largest. However, their intensities in the 1PA spectrum are completely different—the most intense peak corresponds to the third group and has a maximum at about 7.5 eV, the first peak has much lower intensity, and the second cluster of states gives rise to a shoulder in between the first and the third peaks. Such significant difference between the density of states and 1PA intensities is the result of the symmetry-imposed selection rules of the underlying transitions.

Based on the gas-phase calculations, the only bright locally excited state, Σ^+ , lies several eV above the lowest excited state. In the condensed-phase calculations, we found no signatures of this bright $\pi\pi^*$ transition in the eight lowest states—the three states with predominant locally excited $\pi\pi^*$ character have very low oscillator strengths.

The NTO analysis shows that the intense bands in the 1PA spectrum correspond to the states with CTTS character. From Table 2, we see that not all CTTS transitions are bright–among the eight transitions only five are dipole allowed; those are doubly degenerate $\pi \to s$ and $\pi \to p_z$ (with transition dipole moments perpendicular to the molecular axis) and one $\pi \to p_x/p_y$ (with the transition dipole moment parallel to the molecular axis).

Figure 3 shows exciton sizes for the eight states averaged over the equilibrium trajectory.⁵ As one can see, states 3–5 have smaller

TABLE 2 Symmetry analysis of electronic transitions.

Transition	Symmetry/States	# states	1PA allowed
$\pi \rightarrow \pi^*$	$\Pi \times \Pi \to \Sigma^+ + \Sigma^- + \Delta$	4	Σ^+ (z)
$\pi \longrightarrow S$	$\Pi \times \Sigma^+ \longrightarrow \Pi$	2	$\Pi(x,y)$
$\pi \longrightarrow p_z$	$\Pi \times \Sigma^+ \to \Pi$	2	$\Pi (x,y)$
$\pi \rightarrow p_{x}/p_{y}$	$\Pi \times \Pi \to \Sigma^+ + \Sigma^- + \Delta$	4	Σ^+ (z)

Note: The polarization of transitions is shown in parentheses.

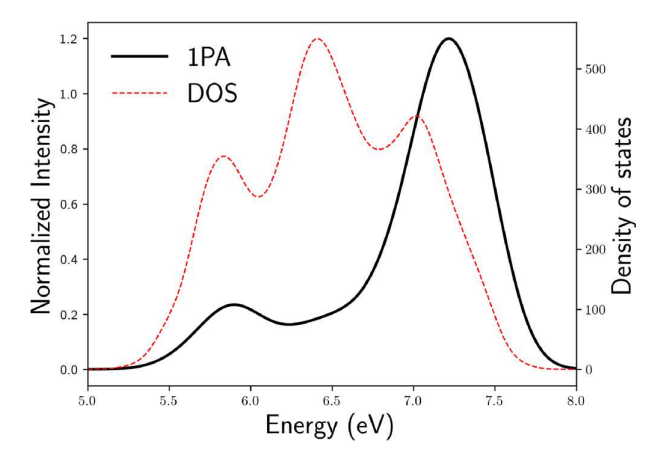


FIGURE 2 Density of states and 1PA spectrum computed using eight states from AIMD snapshots.

sizes, so that they can be classified as predominantly local excitations, whereas states 1–2 and 6–8 have larger sizes. Thus, the lowest eight transitions in our condensed-phase calculations can be described as three dim local excitations, giving rise to the shoulder in the middle, and five brighter states of CTTS character, giving rise to the two brighter peaks, with the brightest peak having the largest CTTS character. Inspection of NTOs (see Tables S2 and S3 in the SI and Reference 5) shows that the third band is dominated by $\pi \to p_x/p_y$ transitions, whereas the lower band is due to $\pi \to s$ transitions. Additionally, the NTOs reveal some mixing between local and CTTS excitations in the two lower bands. We note that this mixing depends strongly on the local structure of the solvent and is not captured by the MD simulations using classical force fields.

Figure 4 summarizes symmetry-imposed selection rules for the manifold of low-lying electronic states in SCN $^-$. Dipole-allowed transitions are those for which product of the irreps of the initial and final state and dipole moment contains fully symmetric irrep (see Table S1 in the SI for help). As one can see, the dipole-forbidden Δ and Σ^- states become two-photon allowed, which should lead to the intensity increase in the low-energy part of the spectrum relative to 1PA.

Figure 5 compares the 1PA and 2PA (σ_{par}) spectra of aqueous SCN $^-$. As one can see, the relative intensities of the three bands change in 2PA, with the lower-energy peaks becoming more prominent, as anticipated from the symmetry considerations. The change becomes even more visible if one takes into account the frequency factor (Figure 5, bottom panel), which favors higher-energy transitions—because the oscillator strength is proportional to ω and the macroscopic 2PA cross section is proportional to ω^2 .

The changes in the intensities result in an apparent red shift of \sim 0.05 eV of the three bands in the 2PA spectrum relative to the 1PA spectrum. This red shift is a purely electronic phenomenon as the position of the excited states are the same in the two calculations, akin to the non-Condon effects observed in fluorescent proteins. ³⁵

To further analyze the 2PA spectrum, we carried out NTO analysis of the 2PA response one-particle transition density

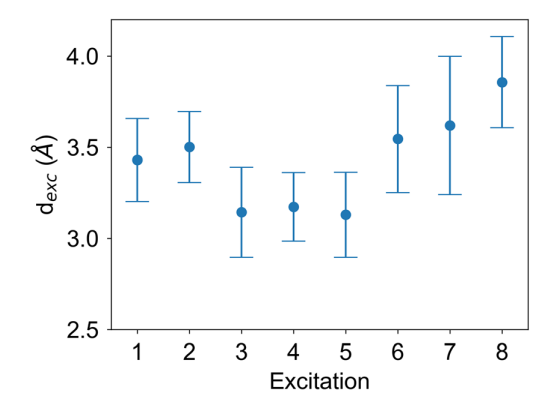


FIGURE 3 Average exciton sizes and standard deviations for the eight lowest states of $SCN^-_{(aq)}$ computed using AIMD snapshots. Reproduced with permission from Reference 5.

1096987x, 2024, 12, Downloaded from https://onlinelibrary.wiley.com/doi/10.1002/jcc.27282 by University Of Southern California, Wiley Online Library on [2103/2024]. See the Terms and Conditions (https://onlinelibrary.wiley.com/terms

on Wiley Online Library for rules of use; OA articles are governed by the applicable Creative Commons

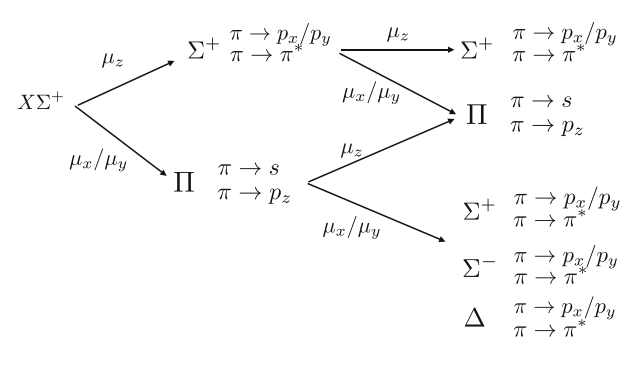


FIGURE 4 Selection rules for 2PA transitions in SCN⁻.

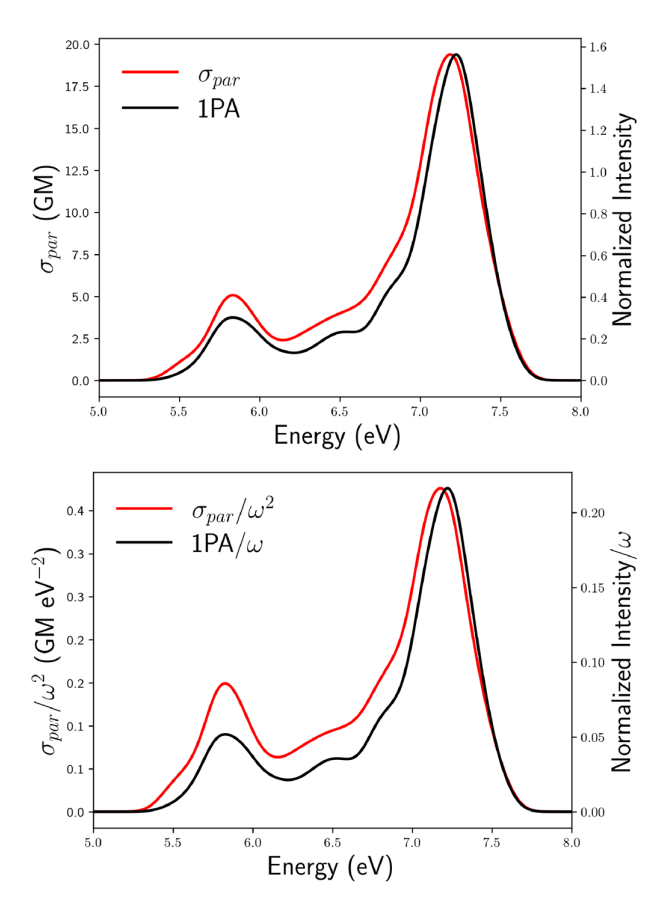


FIGURE 5 Top panel: 1PA and 2PA (σ_{par}) spectra of aqueous SCN $^-$. Bottom panel: Energy-rescaled intensities, i.e., 1PA spectrum divided by the excitation energy (ω) and the 2PA spectrum divided by ω^2 .

matrices (1PTDM).²⁰ Whereas regular NTOs are related to the 1PA intensities, these response (or 2PA) NTOs are related to the magnitude of the 2PA cross sections. Hence, they can reveal the nature of the "virtual" state,³⁶ providing details of the important orbitals involved in the 2PA transition. Tables S2–S11 in the SI show 1PA and 2PA NTOs for a representative snapshot. For this snapshot, the first two transitions have clear *s*-type CTTS character, the next three transitions are

TABLE 3 Structure of 2PA moments for transitions in $C_{\infty v}$ group.¹⁴

Transition	Non-zero elements	Notes ^a
$\Sigma^+ \to \Sigma^+$	M_{zz}, M_{xx}, M_{yy}	$M_{xx} = M_{yy}$
$\Sigma^+ \to \Sigma^-$	M_{xy}, M_{yx}	$M_{xy} = -M_{yx}$
$\Sigma^+ \to \Pi$	$M_{xz},M_{yz},M_{zx},M_{zy}$	$M_{yz} = -iM_{xz}, M_{zy} = -iM_{zx}$
$\Sigma^+ \to \Delta$	$M_{xx},M_{xy},M_{yx},M_{yy}$	$M_{xy} = -iM_{xx}, M_{yy} = -M_{xx}$
		$M_{yx} = -iM_{xx}$

^aThis is valid within Hermitian framework. For Π and Δ , there are two components and their moment are complex-conjugate of each other.

intramolecular, and the last three are *p*-type CTTS transitions. This characterization is based on the analysis of the dominant NTO pair of the 1PA 1PTDMs in Table S2 in the SI.

For the 2PA transitions, the response 1PTDMs have three Cartesian components and depend on frequencies of the two photons, which makes the analysis more involved. Tables S4–S11 in the SI show the 2PA NTOs. Qualitatively, we observe that these NTOs show contributions of multiple "virtual" states into the 2PA cross sections, which are not seen in 1PA NTOs. For example, for the first two transitions (Table S4 in the SI), the response 1PTDMs reveal dominant $\pi \to s$ (CTTS) NTO pair from the *y*-component response 1PTDMs. We also observe a $\pi \to p_x$ (CTTS) character from the less important *x*-component response 1PTDMs.

Symmetry is also responsible for the differences between the 2PA spectra obtained with parallel (σ_{par}) and perpendicular (σ_{perp}) polarized beams. ¹²⁻¹⁴ In general, the ratio is larger for fully symmetric transitions. ¹²⁻¹⁴ Following McClain, ^{11,12} we can estimate the ratio r for our system using idealized symmetry ($C_{\infty V}$). Table 3 summarizes the symmetry-imposed structure of the 2PA moments for the $C_{\infty V}$ group.

For fully symmetric transition, $\Sigma^+ \to \Sigma^+$, we obtain

$$\delta_F = 2S_{xx,xx} + S_{zz,zz} + 4S_{xx,zz} + 2S_{xx,yy}$$
 (14)

and

$$\delta_G = 2S_{xx,xx} + S_{zz,zz}, \tag{15}$$

which yields

$$\begin{split} A &= -(2S_{xx,xx} + S_{zz,zz} + 4S_{xx,zz} + 2S_{xx,yy}) \\ &+ 3(2S_{xx,xx} + S_{zz,zz}) \\ &= 4S_{xx,xx} + 2S_{zz,zz} - 4S_{xx,zz} - 2S_{xx,yy} \\ &= (4S_{xx,xx} + 2S_{zz,zz} + 6S_{xx,zz} + 3S_{xx,yy}) \\ &- (10S_{xx,zz} + 5S_{xx,yy}) \end{split} \tag{16}$$

and

$$\begin{split} B &= 3(2S_{xx,xx} + S_{zz,zz} + 4S_{xx,zz} + 2S_{xx,yy}) \\ &+ 2S_{xx,xx} + S_{zz,zz} \\ &= 8S_{xx,xx} + 4S_{zz,zz} + 12S_{xx,zz} + 6S_{xx,yy} \\ &= 2(4S_{xx,xx} + 2S_{zz,zz} + 6S_{xx,zz} + 3S_{xx,yy}). \end{split}$$
 (17)

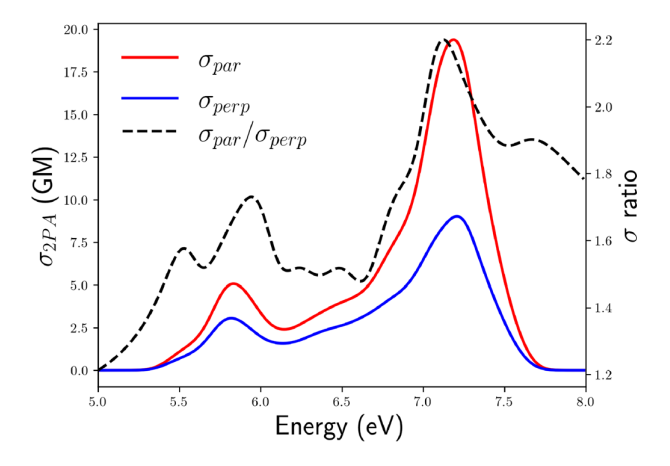


FIGURE 6 Polarization of the 2PA spectra: σ_{par} and σ_{perp} and their ratio.

Neglecting $(10S_{xx,zz} + 5S_{xx,yy})$ terms*, we obtain $B/A \approx 2$, giving rise to $r \approx 3$.

For Σ^- , Π , and Δ transitions, δ_F =0, which gives B/A = 1/3 and r = 4/3.

The computed polarization ratio follows these idealized symmetry-based estimates. The ratio is the largest, reaching the value of 2.2 for the third band, dominated by totally symmetric (Σ^+), $\pi \to p_x/p_y$ transitions. For other transitions, r varies between 1.4 and 1.7. The deviations from the limiting values of 3 (for Σ^+) and 1.3 (for Σ^+ , Π , and Δ) can be explained by mixing configurations of different types, approximations in deriving the limiting values, and by the fact that the two photons are not degenerate.

We conclude by noting that the computed spectra (Figure 6) show that the polarization ratio reveals a more detailed structure than each spectrum alone, with about seven distinct peaks.

4 | CONCLUSIONS

Nonlinear spectroscopies such as 2PA and SFG can provide complementary information of the electronic structure relative to linear (i.e., UV-vis) spectroscopy owing to their different selection rules. By using aqueous thiocyanate, we demonstrated that the symmetry-imposed selection rules of the ideal (isolated) system persist in the condensed-phase and strongly influence 1PA and 2PA spectral features.

We have presented state-of-the-art simulations of the 2PA spectra of $SCN_{(aq)}^-$ and compared it with the 1PA spectrum computed using the same protocol. The simulations reveal changes in the intensity patterns, which can be explained by the native symmetry of the solute. The native symmetry leads to the variations of polarization ratio across the 2PA spectrum, which can facilitate spectroscopic assignments. These changes in the intensities result in an apparent red shift of the 2PA spectrum of 0.05 eV relative to 1PA. We emphasize that the electronic states probed

in both experiments are the same and the shift is of purely electronic nature, akin to non-Condon effects observed in fluorescent proteins. 35

Our study contributes to a growing body of non-linear spectroscopic studies in condensed phase. We hope that our results will inspire future spectroscopic studies on this system and provide useful benchmark for theoretical and experimental developments.

ACKNOWLEDGMENTS

This work was supported by the U.S. National Science Foundation (No. CHE-2154482 to A.I.K.)

CONFLICT OF INTEREST STATEMENT

The authors declare the following competing financial interest(s): Anna I. Krylov is the president and a part-owner of Q-Chem, Inc.

DATA AVAILABILITY STATEMENT

The data that supports the findings of this study are available in the supplementary material of this article

ORCID

Ronit Sarangi https://orcid.org/0000-0002-5838-003X

Kaushik D. Nanda https://orcid.org/0000-0002-3447-6678

Anna I. Krylov https://orcid.org/0000-0001-6788-5016

ENDNOTE

* These terms are neglected for convenience, as was done in other analyzes,²⁷ Analysis of the computed 2PA moments confirms that the neglected terms are indeed small.

REFERENCES

- [1] M. Smith, M. C. R. Symons, Trans. Faraday Soc. 1958, 54, 338.
- [2] G. Stein, A. Treinin, Trans. Faraday Soc. 1959, 55, 1086.
- [3] M. J. Blandamer, M. F. Fox, Chem. Rev. 1970, 70, 59.
- [4] T. R. Griffiths, M. C. R. Symons, Trans. Faraday Soc. 1960, 56, 1125.
- [5] R. Sarangi, K. D. Nanda, A. I. Krylov, Mol. Phys. 2023, 121, e2148582.
- [6] P. B. Petersen, R. J. Saykally, M. Mucha, P. Jungwirth, J. Phys. Chem. B 2005, 109, 10915.
- [7] R. M. Onorato, D. Otten, R. J. Saykally, Proc. Nat. Acad. Sci. 2009, 106, 15176.
- [8] A. M. Rizzuto, S. Irgen-Gioro, A. Eftekhari-Bafrooei, R. J. Saykally, J. Phys. Chem. Lett. 2016, 7, 3882.
- [9] H. Mizuno, A. M. Rizzuto, R. J. Saykally, J. Phys. Chem. Lett. 2018, 9, 4753.
- [10] D. Bhattacharyya, H. Mizuno, A. M. Rizzuto, Y. Zhang, R. J. Saykally, S. E. Bradforth, J. Phys. Chem. Lett. 2020, 11, 1656.
- [11] W. M. McClain, Acc. Chem. Res. 1974, 7, 129.
- [12] M. J. Wirth, A. Koskelo, M. J. Sanders, Appl. Spectr. 1981, 35, 14.
- [13] P. R. Monson, W. M. McClain, J. Chem. Phys. 1970, 53, 29.
- [14] W. M. McClain, J. Chem. Phys. 1971, 55, 2789.
- [15] C. G. Elles, C. A. Rivera, Y. Zhang, P. A. Pieniazek, S. E. Bradforth, J. Chem. Phys. 2009, 130, 084501.
- [16] L. Kjellsson, K. D. Nanda, J.-E. Rubensson, G. Doumy, S. H. Southworth, P. J. Ho, A. M. March, A. Al Haddad, Y. Kumagai, M.-F. Tu, T. Debnath, B. M. Yusof, C. Arnold, W. F. Schlotter, S. Moeller, G. Coslovich, J. D. Koralek, M. P. Minitti, M. L. Vidal, M. Simon, R.



- Santra, Z.-H. Loh, S. Coriani, A. I. Krylov, L. Young, *Phys. Rev. Lett.* **2020**, 124, 236001.
- [17] A. I. Krylov, Annu. Rev. Phys. Chem. 2008, 59, 433.
- [18] K. D. Nanda, A. I. Krylov, J. Chem. Phys. 2015, 142, 064118.
- [19] K. D. Nanda, A. I. Krylov, J. Chem. Phys. 2018, 149, 164109.
- [20] K. D. Nanda, A. I. Krylov, J. Phys. Chem. Lett. 2017, 8, 3256.
- [21] A. V. Luzanov, A. A. Sukhorukov, V. E. Umanskii, Theor. Exp. Chem. 1976, 10, 354 Russian original: Teor. Eksp. Khim., 10, 456 (1974).
- [22] S. A. Bäppler, F. Plasser, M. Wormit, A. Dreuw, Phys. Rev. A 2014, 90, 052521.
- [23] F. Plasser, S. A. Bäppler, M. Wormit, A. Dreuw, J. Chem. Phys. 2014, 141, 24107.
- [24] S. A. Mewes, F. Plasser, A. Krylov, A. Dreuw, J. Chem. Theory Comput. 2018, 14, 710.
- [25] F. Plasser, A. I. Krylov, A. Dreuw, WIREs: Comput. Mol. Sci. 2022, 12, e1595.
- [26] K. D. Nanda, S. Gulania, A. I. Krylov, J. Chem. Phys. 2023, 158, 054102.
- [27] M. de Wergifosse, C. G. Elles, A. I. Krylov, J. Chem. Phys. 2017, 146, 174102.
- [28] M. de Wergifosse, A. L. Houk, A. I. Krylov, C. G. Elles, J. Chem. Phys. 2017, 146, 144305.
- [29] D. Bhattacharyya, Y. Zhang, C. G. Elles, S. E. Bradforth, J. Phys. Chem. A 2021, 125, 7988.
- [30] D. Bhattacharyya, Y. Zhang, C. G. Elles, S. E. Bradforth, J. Phys. Chem. A 2019, 123, 5789.
- [31] K. Sneskov, J. M. H. Olsen, T. Schwabe, C. Hättig, O. Christiansen, J. Kongsted, Phys. Chem. Chem. Phys. 2013, 15, 7567.
- [32] D. Hršak, L. Holmegaard, A. S. Poulsen, N. H. List, J. Kongsted, M. P. Denofrio, R. Erra-Balsells, F. M. Cabrerizo, O. Christiansen, P. R. Ogilby, Phys. Chem. Chem. Phys. 2015, 17, 12090.
- [33] E. Epifanovsky, A. T. B. Gilbert, X. Feng, J. Lee, Y. Mao, N. Mardirossian, P. Pokhilko, A. F. White, M. P. Coons, A. L. Dempwolff, Z. Gan, D. Hait, P. R. Horn, L. D. Jacobson, I. Kaliman, J. Kussmann, A. W. Lange, K. U. Lao, D. S. Levine, J. Liu, S. C. McKenzie, A. F. Morrison, K. D. Nanda, F. Plasser, D. R. Rehn, M. L. Vidal, Z.-Q. You, Y. Zhu, B. Alam, B. J. Albrecht, A. Aldossary, E. Alguire, J. H. Andersen, V. Athavale, D. Barton, K. Begam, A. Behn, N. Bellonzi, Y. A. Bernard, E. J. Berquist, H. G. A. Burton, A. Carreras, K. Carter-Fenk, R. Chakraborty, A. D. Chien, K. D. Closser, V. Cofer-Shabica, S. Dasgupta, M. de Wergifosse, J. Deng, M. Diedenhofen, H. Do, S. Ehlert, P.-T. Fang, S. Fatehi, Q. Feng, T. Friedhoff, J. Gayvert, Q. Ge, G. Gidofalvi, M. Goldey, J. Gomes, C. E. González-Espinoza, S. Gulania, A. O. Gunina, M. W. D. Hanson-Heine, P. H. P. Harbach, A. Hauser, M. F. Herbst, M. Hernández Vera, M. Hodecker, Z. C.

Holden, S. Houck, X. Huang, K. Hui, B. C. Huynh, M. Ivanov, Á. Jász, H. Ji, H. Jiang, B. Kaduk, S. Kähler, K. Khistyaev, J. Kim, G. Kis, P. Klunzinger, Z. Koczor-Benda, J. H. Koh, D. Kosenkov, L. Koulias, T. Kowalczyk, C. M. Krauter, K. Kue, A. Kunitsa, T. Kus, I. Ladjánszki, A. Landau, K. V. Lawler, D. Lefrancois, S. Lehtola, R. R. Li, Y.-P. Li, J. Liang, M. Liebenthal, H.-H. Lin, Y.-S. Lin, F. Liu, K.-Y. Liu, M. Loipersberger, A. Luenser, A. Manjanath, P. Manohar, E. Mansoor, S. F. Manzer, S.-P. Mao, A. V. Marenich, T. Markovich, S. Mason, S. A. Maurer, P. F. McLaughlin, M. F. S. J. Menger, J.-M. Mewes, S. A. Mewes, P. Morgante, J. W. Mullinax, K. J. Oosterbaan, G. Paran, A. C. Paul, S. K. Paul, F. Pavošević, Z. Pei, S. Prager, E. I. Proynov, Á. Rák, E. Ramos-Cordoba, B. Rana, A. E. Rask, A. Rettig, R. M. Richard, F. Rob, E. Rossomme, T. Scheele, M. Scheurer, M. Schneider, N. Sergueev, S. M. Sharada, W. Skomorowski, D. W. Small, C. J. Stein, Y.-C. Su, E. J. Sundstrom, Z. Tao, J. Thirman, G. J. Tornai, T. Tsuchimochi, N. M. Tubman, S. P. Veccham, O. Vydrov, J. Wenzel, J. Witte, A. Yamada, K. Yao, S. Yeganeh, S. R. Yost, A. Zech, I. Y. Zhang, X. Zhang, Y. Zhang, D. Zuev, A. Aspuru-Guzik, A. T. Bell, N. A. Besley, K. B. Bravaya, B. R. Brooks, D. Casanova, J.-D. Chai, S. Coriani, C. J. Cramer, G. Cserey, A. E. DePrince, R. A. DiStasio, A. Dreuw, B. D. Dunietz, T. R. Furlani, W. A. Goddard, S. Hammes-Schiffer, T. Head-Gordon, W. J. Hehre, C.-P. Hsu, T.-C. Jagau, Y. Jung, A. Klamt, J. Kong, D. S. Lambrecht, W. Liang, N. J. Mayhall, C. W. McCurdy, J. B. Neaton, C. Ochsenfeld, J. A. Parkhill, R. Peverati, V. A. Rassolov, Y. Shao, L. V. Slipchenko, T. Stauch, R. P. Steele, J. E. Subotnik, A. J. W. Thom, A. Tkatchenko, D. G. Truhlar, T. Van Voorhis, T. A. Wesolowski, K. B. Whaley, H. L. Woodcock, P. M. Zimmerman, S. Faraji, P. M. W. Gill, M. Head-Gordon, J. M. Herbert, A. I. Krylov,

- [34] A. I. Krylov, P. M. W. Gill, WIREs: Comput. Mol. Sci. 2013, 3, 317.
- [35] E. Kamarchik, A. I. Krylov, J. Phys. Chem. Lett. 2011, 2, 488.
- [36] A. I. Krylov, J. Chem. Phys. 2020, 153, 080901.

J. Chem. Phys. 2021, 155, 084801.

SUPPORTING INFORMATION

Additional supporting information can be found online in the Supporting Information section at the end of this article.

How to cite this article: R. Sarangi, K. D. Nanda, A. I. Krylov, J. Comput. Chem. **2024**, 45(12), 878. https://doi.org/10.1002/jcc.27282